Check for updates

Rapid computational cell-rotation around arbitrary axes in 3D with multi-core fiber

Jiawei Sun,[1,2,*] **Nektarios Koukourakis,**[1,2] **Jochen Guck,**[3,4] **and Jürgen W. Czarske**[1,2,4]

[1]*Laboratory of Measurement and Sensor System Technique, TU Dresden, Helmholtzstrasse 18, 01069 Dresden, Germany*
[2]*Competence Center for Biomedical Computational Laser Systems (BIOLAS), TU Dresden, Dresden, Germany*
[3]*Max Planck Institute for the Science of Light, Staudtstrasse 2, 91058 Erlangen, Germany*
[4]*Cluster of Excellence Physics of Life, TU Dresden, Dresden, Germany*
[*]jiawei.sun@tu-dresden.de

Abstract: Optical trapping is a vital tool in biology, allowing precise optical manipulation of nanoparticles, micro-robots, and cells. Due to the low risk of photodamage and high trap stiffness, fiber-based dual-beam traps are widely used for optical manipulation of large cells. Besides trapping, advanced applications like 3D refractive index tomography need a rotation of cells, which requires precise control of the forces, for example, the acting-point of the forces and the intensities in the region of interest (ROI). A precise rotation of large cells in 3D about arbitrary axes has not been reported yet in dual-beam traps. We introduce a novel dual-beam optical trap in which a multi-core fiber (MCF) is transformed to a phased array, using wavefront shaping and computationally programmable light. The light-field distribution in the trapping region is holographically controlled within 0.1 s, which determines the orientation and the rotation axis of the cell with small retardation. We demonstrate real-time controlled rotation of HL60 cells about all 3D axes with a very high degree of freedom by holographic controlled light through an MCF with a resolution close to the diffraction limit. For the first time, the orientation of the cell can be precisely controlled about all 3D axes in a dual-beam trap. MCFs provide much higher flexibility beyond the bulky optics, enabling lab-on-a-chip applications and can be easily integrated for applications like contactless cell surgery, refractive index tomography, cell-elasticity measurement, which require precise 3D manipulation of cells.

1. Introduction

Optical traps are powerful tools to manipulate and move objects ranging in size from nano- to micron-scales. They are widely applied in biology to manipulate cells in a contact-free manner. The most common optical traps are optical tweezers (OT) [1]. In OTs the dominant force component is the gradient force. Therefore, a steep intensity gradient is required, which can be achieved by sharply focusing the light with a high numerical aperture (NA) microscope objective, mainly in free-space setups. This is accompanied by a small working distance of microscope objectives, which can be a limitation. Holographic optical tweezers (HOT) using spatial light modulators (SLM) originally employed micro-fabricated diffractive optical elements [2] to create multiple traps. The technological progress of SLM boosted the technique's applicability, as it enabled precise wavefront shaping and optical manipulation by holographic control [3–6]. This made optical trapping a vital tool for polymer and small cell manipulation in biotechnology, nanotechnology, and manufacturing [7–11]. However, a high NA is required for stable trapping, which can cause photodamage on the biological sample due to the high laser intensity in the trapping region [12]. The risk of photodamage is strongly reduced in dual-beam traps [13] by trapping the object with two counter-propagating divergent or moderately focused beam with low

NA [14,15]. Dual-beam traps are usually implemented based on optical fibers, providing higher flexibility and can be easily implemented into lab-on-a-chip systems [16,17].

Optical fibers are widely employed in optical manipulation for higher penetration depth and lab-on-a-chip applications [17–25]. Holographic optical manipulation of micro-particles with a size of $1.5\mu m$ through a customized multimode fiber shows the potential of optical manipulation in deep tissues [18]. To manipulate cells much larger than the wavelength, dual-beam traps are realized with two single-mode fibers, having the advantage that they can be easily integrated for lab-on-a-chip applications [17,22]. The first one-dimensional optical manipulation of cells was done by the optical stretcher [19–21]. Two-dimensional (2D) optical manipulation, which rotates the cell about the microscopic optical axis, was realized by mechanical misalignment of the two beams in a dual-beam fiber trap. The so-called fiber-optic spanner consists of two opposing fibers with a slight misalignment, which leads to rotation of the trapped sample [26–28]. Further cell-rotation about the micro-channel's axis was realized by inducing pressure on one of the fibers in the vertical direction [29]. However, the flexibility of these techniques is strongly limited by the precision of the mechanical components, and the vibrations from the mechanical movement can degrade the stability of the system [25]. To overcome the drawbacks of mechanical movement, a holographic controlled cell-rotation about the optical axis of fiber was achieved with few-mode fibers [23,24]. Nevertheless, the linear and angular displacement of the above-mentioned dual-beam manipulation techniques are still large. Stable rotation of cells is achieved by combining dual-beam trap with microfluidic techniques [29–32]. The cell is trapped slightly off the middle of a microchannel, and a flowing medium induces the rotation due to the force gradient acting on the cell. The system can be run with a continuous flow to increase the system's stability and throughput. Dielectrophoretic cell rotation [33] was proposed with lab-on-a-chip systems, however, this approach strongly depends on particles' electrical properties. In-plane and out-of-plane rotation of cells were achieved by acoustic microstreaming using two different configurations [34,35]. This approach shows a wide range of rotation capability for biological samples ranging from micrometer to submillimeter scale. However, these approaches can only rotate the cell about less than two axes, and the targeted and repeatable orientation of the cell is difficult to achieve. Up to now, a device that can fully control the rotation of a large biological cell about all three axes in 3D is currently not available.

For the first time, we propose a flexible and stable 3D cell rotation approach with an adaptive phased-array optical manipulator (PAOM). The PAOM is based on a modified dual-beam trap (Fig. 1(a)), consisting of a commercially available MCF in conjunction with a single-mode fiber (SMF). Due to initial optical path differences between cores, plane-waves propagating in MCFs
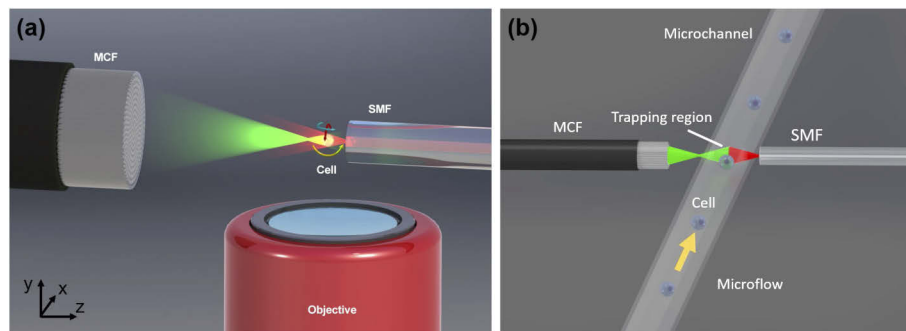
Fig. 1. (a) The 3D illustration shows a biological cell is rotated about X-,Y-and Z- axis with the PAOM, which consists of a multi-core fiber bundle and an opposing single-mode fiber. (b) 3D illustration demonstrates the workflow of the PAOM. Cells are delivered to the trapping region by the microflow.

result in a speckled output in the ROI, which is 600 μm away from the distal fiber facet. These path differences can be corrected by calibration employing DOPC [36,37]. In our previous work, in-situ calibration approaches based on digital phase conjugation (Fig. 2(b)) are demonstrated to overcome the phase distortion in MCFs [38,39]. Therefore, an MCF can be transformed into a phased array by holographic control of phase and amplitude of the light wave exiting the individual cores (Fig. 2). The PAOM is thus capable to real-time control the intensity distribution in the ROI with high fidelity and by this achieve a targeted orientation of a biological cell about any axis in 3D. Miniature multi-core fibers with diameters of 350 μm enable the integration of the PAOM to a microfluid channel (Fig. 1(b)), promising high throughput non-contact optical manipulation of biological cells.
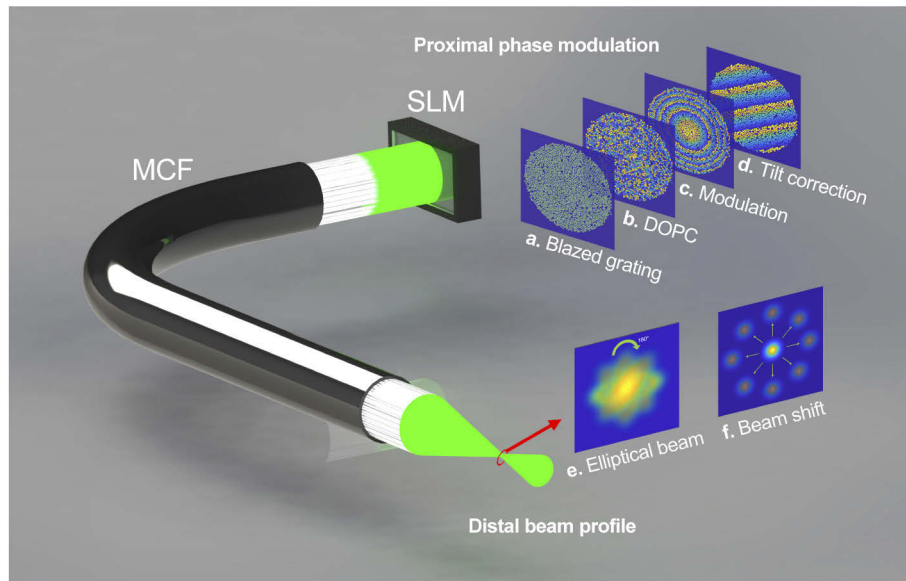

Fig. 2. Illustration of the adaptive phased-array optical manipulator (PAOM). A superposition of phase masks is imaged on the proximal facet of the MCF for holographic control of the beam profile at the ROI. (a) Each core is modulated in a corresponding circular area on the SLM, blazed gratings are superposed on each circular area. (b) Digital optical phase conjugation (DOPC) pre-compensates the phase distortion in the MCF. (c) The modulation layer displays the phase modulation holograms for the tailored output of the MCF. (d) Phase modulation to correct the tip and tilt of the output beam of the MCF. (e) The rotating elliptical beam at the MCF output rotates the cell about Z-axis in PAOM. (f) Lateral beam-shift induces rotation of cell about the other 3D axes in PAOM.

2. Controlled rotation of cells about an arbitrary axis in 3D

2.1. Transform a multi-core fiber into a phased-array

We transform a 50 cm commercially available MCF (FIGH-350S; Fujikura) with 10,000 cores and a core-to-core distance smaller than 3μm, into a phased array, using the experimental setup depicted in Fig. 3.

The laser beam from a 532-nm diode-pumped laser is expanded by a 4-f configuration (L2-L3) to fully use the active area of the SLM (PLUTO LCOS SLM, Holoeye Photonics). Light coupled in each fiber core is modulated by a corresponding circular area on the SLM. Due to the cladding area is not illuminated, the crosstalk between cores is suppressed and the quality of the phase modulation is increased. Blazed gratings are superposed on each circular area (Fig. 2(a)) for
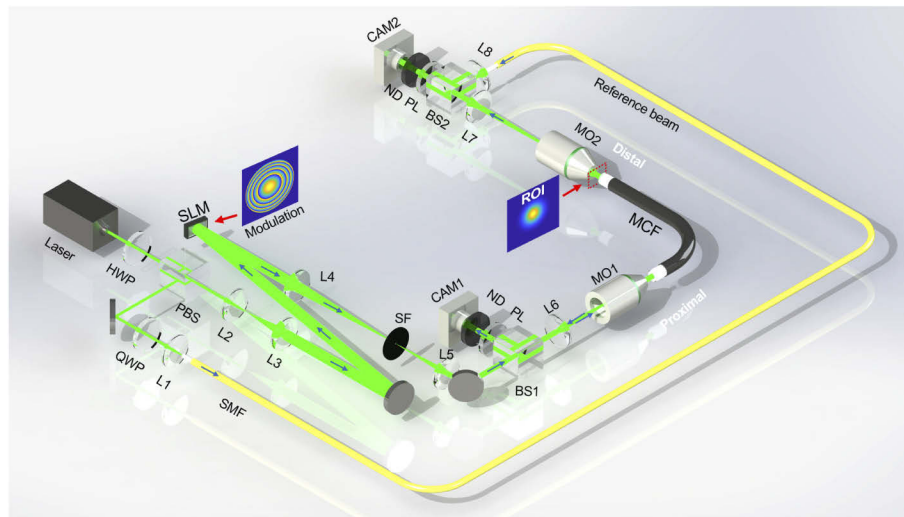
Fig. 3. Sketch of the experimental setup for calibration and beam profile control of an MCF. Laser, diode-pumped solid-state (DPSS) laser. HWP, half-wave plate; PBS, polarizing beam splitter cube; SLM, spatial light modulator; L1-L8, lenses; SF, spatial filter; BS1, 10:90 beamsplitter cube; BS2, 50:50 beamsplitter cube; PL, polarizers; ND, neutral density filters; CAM1, CAM2, CMOS cameras; MO1, MO2, microscope objectives; QWP, quarter-wave plate. Red marked area shows a moderate focus generated at the ROI for optical trapping by the phase modulation on the SLM. The blue arrows indicate the propagation direction of the laser beam.

higher diffraction efficiency, resulting in higher intensity in the first diffraction order. The first order transmits through an iris diaphragm (shown as SF in Fig. 3) in the Fourier plane of a 4-f system (L4-L5), while all the other diffraction orders from the SLM are filtered out, which reduces the influence of unwanted diffraction background [40–42]. The phase modulation, which is contained in the first order, is projected on the proximal fiber facet by a compact microscope system including a microscope objective (MO1; 20X Plan Achromat Objective, 0.4 NA, Olympus). The proximal facet of the MCF is back-projected on the CAM1 (uEye camera, IDS), shown in Fig. 3, to monitor the modulation input of the MCF, ensuring the phase modulation is exactly projected on the fiber facet.

The individual cores have different optical path-lengths, which distorts the phase information of the light propagating through the MCF [43]. We use digital holography [44] to measure this distortion. The reference beam is split from the same laser source by a polarizing beam splitter (shown as PBS in Fig. 3). The power ratio of reference- and object beam can thus be easily adjusted by rotating the half-wave plate (HWP). In order to remove the back-reflected light when coupling the beam into the SMF, a quarter-wave plate (QWP) is introduced and rotated to 45°. The distal fiber facet is projected on the CMOS camera (CAM2; uEye camera, IDS) by the microscope system (MO2, L7), and interferes there with the collimated reference beam. Neutral density filters (NE50, Thorlabs) are mounted on cameras to avoid overexposure. The digital off-axis hologram (Fig. 4(a-c)) is used to determine the phase difference between the cores. To compensate for the phase delay, the measured phase of each core on the camera (CAM2) was conjugated and affine transformed into the SLM coordinate system. If the phase conjugate is displayed on the SLM, it pre-deforms the wavefront and corrects the phase distortion of the MCF (Fig. 4(d-f)). A precise beam control for stable trapping and rotation requires a high-quality calibration, leading to a high peak-to-background ratio and accurate beam forming in the ROI.
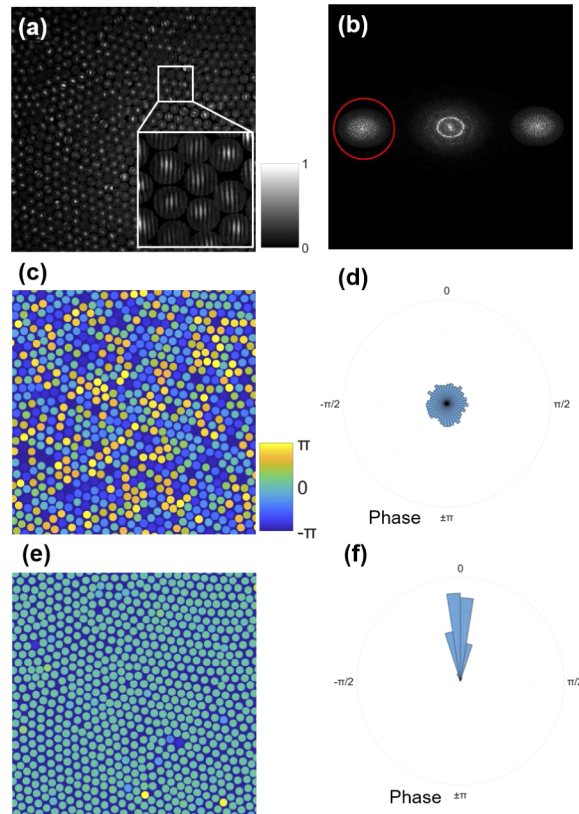
Fig. 4. The calibration process of the MCF. (a) Off-axis digital hologram of the MCF's fiber facet captured on CAM2. (b) Fourier transformed spectrum image of the captured hologram, two first-order terms are separated from the off-axis holography. Red marked area denotes one of the first order terms cropped in the spectrum image for phase reconstruction. (c) The reconstructed phase of cores from the captured hologram before calibration, denoting a random phase distribution of cores. (d) The polar histogram shows a quantitative evaluation of the phase distribution of cores. The length of bars in the polar histogram indicates the number of cores that are in the same phase range. (e) The reconstructed phase of cores from the captured hologram after calibration with DOPC, demonstrating the phase distortion is compensated by the DOPC. (f) The polar histogram shows 93.75% of used cores' phase are compensated to the range of [-π/8, π/8].

2.2. Dual-beam trap with multi-core fiber

To form a dual-beam trap, the MCF functions as a phased array. The compensating phase map is superimposed by a tailored Fresnel lens (Fig. 5(a)) and displayed on the SLM to individually modulate the phase of each core for generating a moderately focused beam which has a low NA (Fig. 5(b)). We assume that the total magnification ratio from the SLM to the phased-array is M, the pixel pitch of the SLM is a and the center of the Fresnel lens located at (x_0, y_0). To generate a moderately focused beam with a focal distance of f, the phase modulation value $\phi(x, y)$ for the core centered at (x, y) in the SLM coordinate system can be described as

$$\phi(x, y) = mod\left(\frac{\pi a M}{2 f \lambda}[(x - x_0)^2 + (y - y_0)^2], 2\pi\right), \tag{1}$$
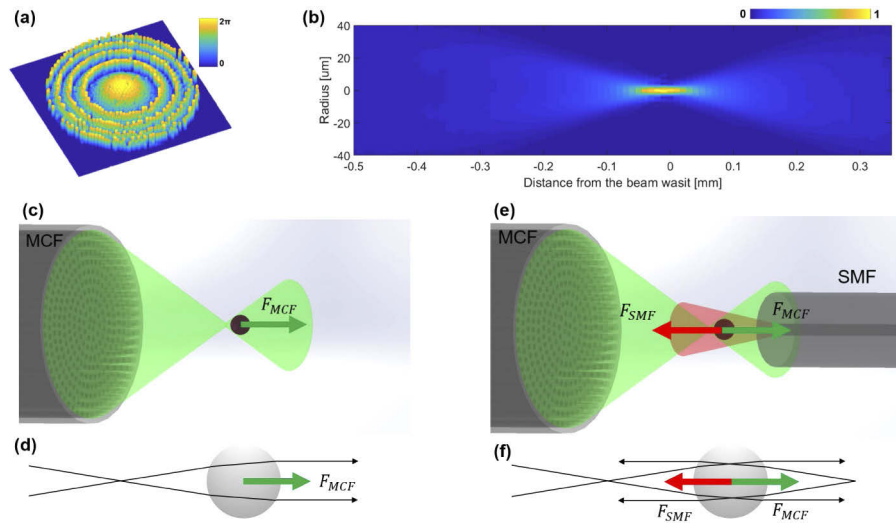
Fig. 5. (a)The 3D plot of the tailored Fresnel lens for the PAOM. (b) Holographic axial amplitude slice at the center of the beam from PAOM. This focus is generated at 600 μm away from the fiber facet with a very high peak-to-background ratio of 29dB. (c) Illustration shows a biological cell in the divergent part of the beam. (d) The scattering force on the cell acts along the transverse direction. The black arrow represents the light ray transmitting through the cell. (e) Illustration shows a biological cell trapped in the PAOM. (f) The scattering forces from both beams cancel out.

The moderately focused beam leads to the scattering force induced by momentum-transfer from light to matter toward the transverse beam propagation direction (Fig. 5(c,d)). The opposing divergent beam from the SMF (780HP, 0.13 NA, Thorlabs) induces the force toward the opposite direction (Fig. 5(e)). The cell is trapped stably when the forces cancel out (Fig. 5(f)). The laser power from each fiber is below 40mW to avoid photodamge or thermal change. The object can be trapped with high stiffness when the NAs and intensity of both beams is equal, which indicates the focal length f of the Fresnel lens

$$f = \frac{d}{2\,NA_{SMF}}, \tag{2}$$

where d is the the modulated area's diameter of the MCF.

Conventional embedded dual-beam traps consisting of two single- or multi-mode fibers [17,19,23,24] are fixed on the chip. To obtain a stable optical trap, the two fibers should share the

same optical axis. Any slight tilt of the fibers will degrade the quality of the trap. To compensate for such slight tilts, our PAOM has the capability to further superposing an adaptive tilt correction phase image (Fig. 2(d)) on the SLM phase modulation.

### 2.3.　Dynamic modulation of PAOM orientates the cell about the fiber axis

In order to rotate a biological cell about the fiber-axis (Z-axis), a dynamically controlled asymmetric beam has to be employed. However, precise beam profile control in the trapping region close to the diffraction limit is an obstacle. It has been demonstrated that the rotation of a double-lobe mode from a few-mode fiber can facilitate the orientation of cells about this axis [24]. Nevertheless, the double-lobe beam profile is asymmetric to the opposing Gaussian beam profile emitting from the SMF, which may induce further unbalanced gradient force. The intensity distribution of the two lobes has to be precisely equal to cancel out the gradient force and not induce unwanted cell rotation around undesired axes or further movement between the lobes.

We employ a dynamic modulated elliptical beam profile (Fig. 6(a)) to overcome this problem. Due to the near Gaussian distribution of the elliptical beam profile during rotation, the scattering force is canceled out in the manipulation process. Therefore, this tailored beam profile, in principle, can avoid lateral movement of the cell during the rotation (Fig. 6(b)). The direction of the gradient force will point in a direction to draw the area of high refractive index of the cell into the area of high intensity of the beam [24,26]. Hence, a cell with heterogeneous refractive index distribution or non-spherical shape follows the rotation of the beam (Fig. 6(c)). To specify, the scattering forces from both fibers are canceled out in Z-axis. In each rotation step, the elliptical beam from the MCF is rotated for 1° about the Z-axis, the net torque from the gradient force rotates the cell toward the same direction. The gradient force decreases when the cell rotates to the maximum overlap position. The opposing frictional torque from the surrounding liquid slows down the rotation until the net torque from the gradient force is larger than the static frictional torque.

$$\phi_e(x, y) = mod\left(\frac{\pi a M}{2f\lambda}[(1 + \beta)(x - x_0)^2 + (y - y_0)^2], 2\pi\right). \tag{3}$$

Previously reported wavefront shaping with phase modulation mostly uses Gerchberg-Saxton algorithm [24,45,46], which is an iterative phase retrieval algorithm. This approach takes more than 10 s for calculating a single phase modulation image in our setup [47]. To achieve real-time generation of the elliptical Gaussian beam profile, the Fresnel lens is "stretched" by a deformation factor of β along the X-axis. Therefore, the modified Fresnel lens (Fig. 6(d)) can be described as

Compared to the iterative phase retrieval algorithms, the simplicity of our approach (Eq. 3) enables real-time holographic control of the beam profile. It takes just 0.02 s to generate one phase modulation image, and can be even faster with GPU acceleration. The elliptical beam aspect ratio can be precisely manipulated by simply changing the deformation factor β for various applications. The phase modulation image is rotated about the center of the Fresnel lens (x_0, y_0), which determines the orientation of the elliptical beam. The corresponding phase modulation value for the phased-array is sampled from the modified Fresnel lens (Fig. 6(e)). Continuous and homogeneous rotation of the elliptical beam profile from 0° to 360° in 1°-steps is captured by the camera (CAM2) (see Visualization 1). As shown in Fig. 6(f), the detected experimental rotation angle of the beam profile fits the modulation angle very well. A small shape vibration of the beam profile is characterized by the full-width half-maximum (FWHM) of the minor and major axis (Fig. 6(g,h)), with a mean deviation of 2% and 5%, respectively. The intensity homogeneity is crucial for a stable rotation of the cell because it determines the scattering force. The mean deviation of the averaged amplitude distribution at each angle is only 4% over a full 360° rotation. The homogeneous rotation of the elliptical beam profile enables the robust control of the cell's orientation.
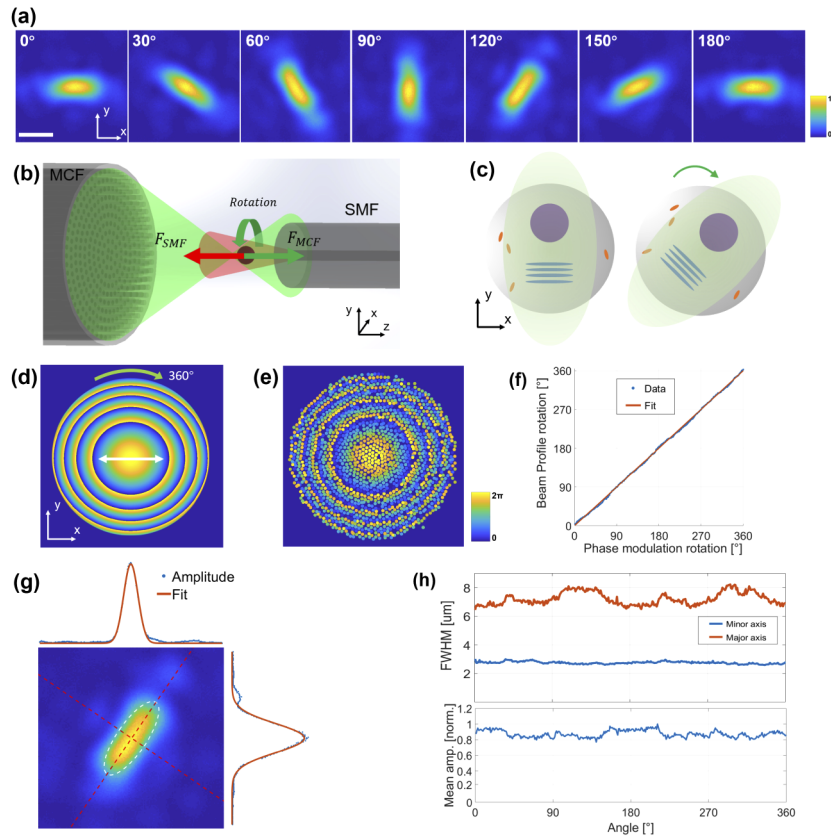
Fig. 6. (a) Selected frames from a full 360° rotation of the elliptical beam profile, the scale bar indicates a length of 5μm (see Visualization 1). (b) Illustration shows a biological cell was rotated about the fiber axis by the gradient force induced by the rotation of the elliptical beam in the PAOM. The direction of rotation is denoted by the green arrow. (c) Due to the heterogeneous internal refractive index distribution, the cell follows the rotation of the elliptical beam. The green arrow indicates the direction of rotation. (d) A "stretched" Fresnel lens calculated from Eq. 3 are rotated for 360° to orientate the elliptical beam profile. White arrow indicates the "stretching" direction of the Fresnel lens for creating the elliptical beam profile. (e) Phase modulation value for each core is transferred to the phased-array. (f) Measured rotation angle of the beam profile and the corresponding rotation angle of the phase modulation. (g) The white dashed line indicates the fitted ellipse, and the red dashed lines indicate the major and minor axis of this ellipse, respectively. Beside the image is the Gaussian fitted amplitude distribution along the minor and major axis respectively. (h) Full-width half maximum (FWHM) of the major and minor axis and the normalized mean amplitude distribution of the beam profile at each rotation angle.

The PAOM is integrated to a microscope with a long working distance objective (50X, 0.42 NA, Mitutoyo) to observe the rotation of the cell (Fig. 7(a,b)). Shortpass filters (FES0500, Thorlabs) are mounted in front of the camera to remove the scattered light from optical manipulation. Visualization 2 demonstrates a step-controlled rotation of an HL60 cell which is recorded on CAM3 (Ueye CP, IDS). The speed of the video is modified to 7.5x to show the rotation process better. The selected frames in Fig. 7(c) shows a full-180° rotation of the cell. To quantitative evaluate the rotation, the distance of the marked features (Fig. 7(c)) to the center of cell is measured on the 2D images. The cell is considered as a perfect sphere, therefore the cell orientations in the selected frames, which is shown in Fig. 7(d), can be calculated from the lateral shift to the center of cell. The error bar indicates the calculated angle deviation caused by the diffraction limit. The cell was rotated at a constant angular speed, and its orientation follows the rotation of the elliptical beam.
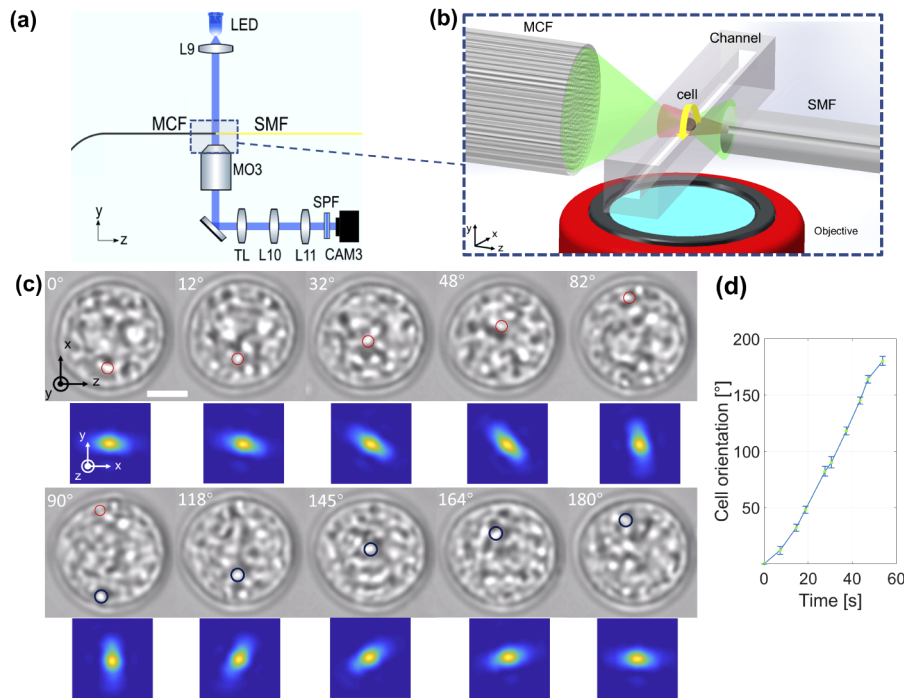

Fig. 7. (a) Optical setup for observing the rotation of cells. L9-L11, lenses; MO3, microscope objective; TL, tube lens; SPF, shortpass filter; CAM3, CMOS camera. (b) 3D illustration of the marked area in (a). (c) Microscopic image frames recorded on CAM3 in the first and third row show a controlled rotation of an HL60 cell about the fiber axis (Z-axis) (see Visualization 2). The rotation angle is calculated by the red and blue marked unique feature on the cell. The scale bar represents a length of 5μm. The corresponding elliptical beam profiles at the beam waist which are demonstrated in the second and fourth row . (d) The orientation of the cell is almost linearly proportional to the time, which shows a uniform rotation.

2.4. Controlled cell-rotation about an arbitrary axis in 3D

We have demonstrated that biological cells can be rotated about the Z-axis by holographic controlled rotating elliptical beam profile. To achieve cell-rotation about the other two axes in the PAOM, we demonstrate an approach that rotates the cell about the X- and Y-axis by lateral shifting the beam emitted from the MCF (Fig. 8(a)). The net torque from optical forces induces

the rotation, and the cell rotates at a constant angular speed when the resultant torque from optical forces and the opposing friction force from the surrounding liquid is zero. To be more specific, due to the gradient force always pointing toward the area of highest light intensity for an object with higher refractive index than surrounding, lateral shift of the beam waist (Fig. 8(b)) induces a resultant gradient force toward the shift direction (Fig. 8(c)). This gradient force cause the movement the cell to the position where the gradient forces from both beams are canceled out in longitude direction (Fig. 8(d)). The action point of both scattering forces $\vec{F}_{MCF}$, $\vec{F}_{SMF}$ shifts from the center of gravity by a distance of $\vec{r_1}$, $\vec{r_2}$, respectively. This net torque from both scattering forces induces the rotation of the cell. Due to the relatively rough surface of the cell, the frictional torque $\vec{\tau}_{friction}$ from the surrounding liquid is not neglectable. The resultant torque $\vec{\tau}$ caused by the two opposing transverse scattering forces and the friction force can be described as

$$\vec{\tau} = \vec{\tau}_{MCF} + \vec{\tau}_{SMF} - \vec{\tau}_{friction} = \vec{r_1} \times \vec{F}_{MCF} + \vec{r_2} \times \vec{F}_{SMF} - \vec{\tau}_{friction}. \qquad (4)$$
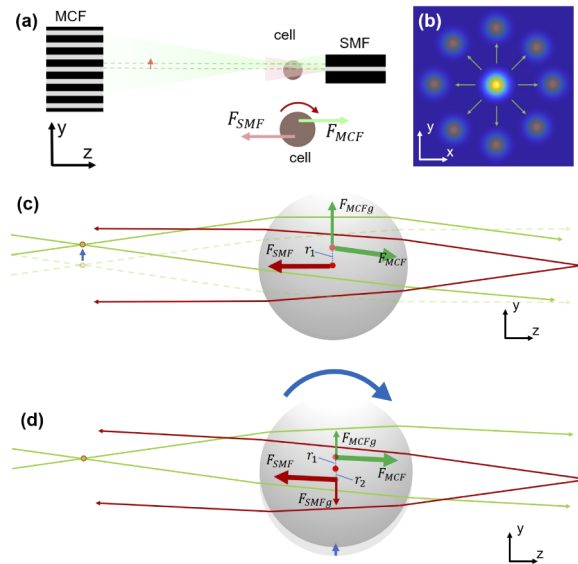
Fig. 8. (a) 2D slice in Y-Z plane shows a biological cell is rotated about the X-axis by shift the beam in the Y-axis direction. (b) The intensity profile of the beam waist in the X-Y plane demonstrates the lateral shift of the beam in all directions. (c) Sketch of the scattering and gradient forces of the initial state when the beam from the MCF is shifted in Y-axis direction. (d) The cell moves to the position where gradient forces are canceled out, and the net torque from both scattering forces induces the rotation. The cell rotates at a constant angular speed when the torque from scattering forces is canceled out with the frictional torque from the surrounding liquid. The cell rotates about the X-axis with a constant angular speed.

It causes a change in the angular momentum $\vec{L}$ in the direction of that torque

$$\frac{d\vec{L}}{dt} = \vec{\tau}. \qquad (5)$$

Therefore, the angular acceleration depends on the resultant torque $\vec{\tau}$. When the resultant torque is zero, the cell can rotate with a constant angular speed about the axis perpendicular to the focus shift direction due to the constant angular momentum (Fig. 8(a)). However, the offset distance needs to be tailored for cells with different diameters and shapes to keep the

cell rotating about its pivot position. Cells with larger size have larger static friction, therefore larger torque from both fibers is required to start the rotation. According to Eq. 4, increasing the offset distance can increase the torque from fibers to rotate larger cells. It has to be noted that further increase the offset distance from the tailored position can induce spiral rotation or even orbital rotation [48,49]. Therefore, precise manipulation of the beam in all directions with a sub-micrometer precision is required. Increasing the laser power can be an alternative solution, but the power from both fibers has to be increased simultaneously to avoid lateral movement. In principle, this approach is an advanced version of the optical spanner [28,29], which is based on mechanical misalignment of two SMFs to induce a rotation. The PAOM enables introducing this misalignment digitally in all directions and thus allows for rotation in three dimensions.

In order to have precise control of the beam offset, we use variables m_x, m_y which determines the lateral shift of the Fresnel lens center (x_0, y_0) in X- and Y-axis, respectively,

$$\phi_s(x, y) = mod \left\{ \frac{\pi a M}{2f\lambda} \left([x - (x_0 + m_x)]^2 + [y - (y_0 + m_y)]^2 \right), 2\pi \right\}. \tag{6}$$

The minimum travel step of m_x, m_y is the pixel pitch of the SLM, which is 90 nm at the trapping region in our setup. The beam modulated by the phased-array can move in all directions in the X-Y plane by program control. The supplementary video (see Visualization 3) captured by the camera (CAM2) demonstrates the real-time program controlled beam movement. Fig. 9(a) is the trajectory of the real-time holographic controlled movement of the beam waist, which shows the high fidelity of the beam motion control. The intensity stability is crucial for maintaining the balance of scattering forces. The mean amplitude in Fig. 9(b) characterizes a very high intensity stability in the beam movement process with a mean deviation of 0.78% and a maximum intensity variation smaller than 5%.
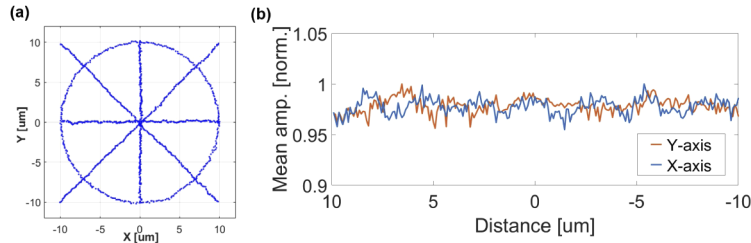
Fig. 9. (a)Trajectory of the beam movement shown in the supplementary video (see Visualization 3). (b) Normalized mean amplitude at the focal spot when the beam is moved in X- and Y- direction, with a mean deviation of 0.78% and a maximum intensity variation smaller than 5%.

To illustrate the real-time cell-motion control capability of the PAOM, an HL60 cell with an irregular shape was trapped for fast identification of the rotation angle (see Visualization 4). The cell is first rotated about the X-axis by precisely shifting the beam to the tailored offset position in Y-direction (Fig. 10(a, b)). When a full-360° rotation is finished, the beam shifts to the tailored offset position in X-direction by real-time program control. This changes the orientation of the cell by 90° about Y-axis (Fig. 10(c, d)). The beam is then switched back to the offset position in Y-direction to further rotate the cell about X-axis (Fig. 10(e, f)). To the best of our knowledge, this is the first time a real-time controlled multi-axis rotation of a biological cell is achieved in a dual-beam trap. It should be noted that the beam can be laterally shifted in any direction in 3D with high fidelity, which means controlled rotation about an arbitrary axis of a cell can be achieved by our approach.
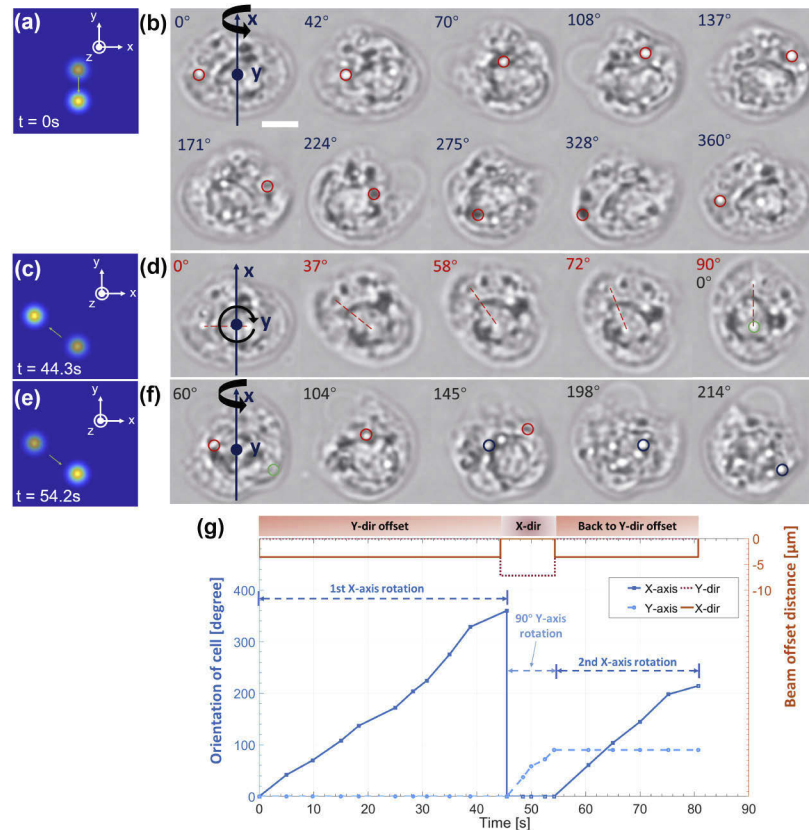
Fig. 10. (a) X-Y plane slice at beam waist of the output from MCF shows the program-controlled shift of the beam in the Y-axis. This induces rotation of the cell about the X-axis. (b) Microscopic image frames in the Y-Z plane (see Visualization 4) show a controlled rotation of an HL60 cell about the X-axis. The rotation angle is calculated by the red marked unique feature on the cell. The scale bar represents a length of $5\mu m$. (c) After the cell is fully rotated about the X-axis, the beam is shifted by real-time program-control to create beam offset in the X-axis. This induces rotation of the cell about the Y-axis. (d) Frames shows rotation about the Y-axis for $90°$. The red dashed line indicates the orientation of the cell. (e) The beam is shifted back to the off-set position in Y-axis. (f) The cell is then rotated about the X-axis for the second time by controlled beam shift to show full spatial information of the cell. (g) Quantitative characterization of program-controlled beam shift in X- and Y-direction and the corresponding rotation angle about X- and Y-axis. The dark blue solid line denotes the cell-rotation angle about X-axis, the light blue dashed line denoting rotation about Y-axis. The orange solid line denotes the controlled offset distance of the beam from MCF in Y-direction, the orange dashed line denoting offset distance in X-direction. This demonstrates that, in the PAOM, the orientation and the rotation axis of the cell can be controlled in real-time.

3. Discussion

To the best of our knowledge, the PAOM is the first dual-beam trap device that can stably rotate cells much larger than the wavelength about all 3D axes in a real-time program-controlled way due to the very high degree of freedom of the direct light delivery of the MCF based phased-array. The simplicity of our phase generation algorithm and the fast response of the modern liquid crystal SLMs enables real-time modulation of the beam profile at the ROI. The entire running time of generating a phase modulation image and displaying it on the SLM can be faster than 0.1 s even with a conventional computer. It can be noticed in the Visualization 4 that there is a 1 s retardation for the cell to change the rotation axis from X- to Y-axis, because when the beam is shifted, the cell always moves to the most stable position where the gradient forces are cancelled out and the torque of the scattering forces is zero before the rotation (Fig. 8(c,d)). This process takes slightly longer time for a large beam shift distance. The cell shown in Fig. 10 has shorter diameter in Y-axis, which means smaller beam shift distance in Y-axis is required for a stable rotation about the X-axis. This leads to a very fast response of less than 0.2 s retardation when the rotation axis is changed back from Y- to X-axis (Fig. 10(g)).

The quality of the cell control is strongly dependent on the quality of the intensity control, which again is affected by the robustness of the calibration. The calibration strongly affects the portion of modulated intensity, which is projected into the trapping region. In this paper, the calibration relied on a transmission geometry, which requires optical access to both fiber ends. In-situ calibration and monitoring could be implemented by a calibration procedure we introduced in [38] to compensate drifts, temporal and bending phase distortion without access to both fiber tips. Alternatively, recent work demonstrates a novel twisted MCF, that shows a performance independent of the fiber bending [50]. In addition, switching the laser source to the near-infrared range with an appropriate MCF can further decrease the risk of photodamage on cells.

With the capability of robust real-time control, the PAOM opens up new perspectives for 3D cell-manipulation in a dual-beam trap. One important application of our work is 3D refractive index tomography, which requires stable sample rotation about two perpendicular axes for full spatial frequency information [31,51,52]. The PAOM can have broader applications beyond the tomography due to the robustness and reproducibility. For instance, the PAOM paves the way to contactless cell surgery [53]. Real-time stable control of cell's orientation about an arbitrary axis in 3D enables laser processing on any desired area on the cell by high-power short-pulse laser. Besides, due to the rather small diameter of $350 \mu m$, the PAOM can be easily integrated into the lab-on-a-chip systems. Moreover, it has to be noted that the optical stretching [19] can also be realized in the PAOM by increasing the power of both beams.

4. Conclusion

We presented a novel and powerful fiber-based dual-beam optical manipulator named PAOM, which rotates the biological cell about all 3 axes in 3D and enables cell-rotation about any 3D arbitrary axis. For the first time, the rotation axis and the orientation of the cells is controlled in real-time by holographic modulated light through a commercially available MCF, the phase modulation can be generated and delivered to the trapping region with latency less than 0.1 s for a conventional PC. DOPC compensates the phase distortion, enabling precise wavefront shaping through the MCF. The rather small size of the optical fibers facilitates their implementations in lab-on-a-chip systems providing high throughput measurements. Our work opens new perspectives for fiber-based dual-beam traps, eliminating the need for any mechanical misalignment for cell manipulation. This work provides very high flexibility for wider applications in advanced microscopy techniques beyond 3D refractive index tomography, for example, Brillouin microscopy [54] to sort the origin of diseases or future cell surgery with the nanoscale precision.

Biomedical Optics EXPRESS

Disclosures. The authors declare no conflicts of interest.

Data availability. Data underlying the results presented in this paper are available from the corresponding author upon request.

References

1. A. Ashkin, J. M. Dziedzic, and T. Yamane, "Optical trapping and manipulation of single cells using infrared laser beams," Nature **330**(6150), 769–771 (1987).
2. D. G. Grier, "A surprisingly attractive couple," Nature **393**(6686), 621–623 (1998).
3. M. Reicherter, T. Haist, E. Wagemann, and H. J. Tiziani, "Optical particle trapping with computer-generated holograms written on a liquid-crystal display," Opt. Lett. **24**(9), 608–610 (1999).
4. K. Kim and Y. Park, "Tomographic active optical trapping of arbitrarily shaped objects by exploiting 3D refractive index maps," Nat. Commun. **8**(1), 15340 (2017).
5. G. Vizsnyiczai, A. Búzás, B. L. Aekbote, T. Fekete, I. Grexa, P. Ormos, and L. Kelemen, "Multiview microscopy of single cells through microstructure-based indirect optical manipulation," Biomed. Opt. Express **11**(2), 945–962 (2020).
6. E. Gerena, F. Legendre, A. Molawade, Y. Vitry, S. Régnier, and S. Haliyo, "Tele–robotic platform for dexterous optical single-cell manipulation," Micromachines **10**(10), 677 (2019).
7. R. Diekmann, D. L. Wolfson, C. Spahn, M. Heilemann, M. Schüttpelz, and T. Huser, "Nanoscopy of bacterial cells immobilized by holographic optical tweezers," Nat. Commun. **7**(1), 13711 (2016).
8. D. G. Grier, "A revolution in optical manipulation," Nature **424**(6950), 810–816 (2003).
9. O. M. Maragò, P. H. Jones, P. G. Gucciardi, G. Volpe, and A. C. Ferrari, "Optical trapping and manipulation of nanostructures," Nat. Nanotechnol. **8**(11), 807–819 (2013).
10. F. Hörner, R. Meissner, S. Polali, J. Pfeiffer, T. Betz, C. Denz, and E. Raz, "Holographic optical tweezers-based in vivo manipulations in zebrafish embryos," J. Biophotonics **10**(11), 1492–1501 (2017).
11. M. Habaza, B. Gilboa, Y. Roichman, and N. T. Shaked, "Tomographic phase microscopy with 180 rotation of live cells in suspension by holographic optical tweezers," Opt. Lett. **40**(8), 1881–1884 (2015).
12. P. Yu, Y. Liu, Q. Zhao, Z. Wang, Y.-M. Li, and L. Gong, "Reducing photodamage in optical trapping of individual cells in living zebrafish," Appl. Phys. Express **13**(3), 032008 (2020).
13. K. C. Neuman, E. H. Chadd, G. F. Liou, K. Bergman, and S. M. Block, "Characterization of photodamage to Escherichia coli in optical traps," Biophys. J. **77**(5), 2856–2863 (1999).
14. A. Ashkin, "Acceleration and trapping of particles by radiation pressure," Phys. Rev. Lett. **24**(4), 156–159 (1970).
15. A. Constable, J. Kim, J. Mervis, F. Zarinetchi, and M. Prentiss, "Demonstration of a fiber-optical light-force trap," Opt. Lett. **18**(21), 1867–1869 (1993).
16. J. Guck, R. Ananthakrishnan, T. Moon, C. Cunningham, and J. Käs, "Optical deformability of soft biological dielectrics," Phys. Rev. Lett. **84**(23), 5451–5454 (2000).
17. P. R. T. Jess, V. Garcés-Chávez, D. Smith, M. Mazilu, L. Paterson, A. Riches, C. S. Herrington, W. Sibbett, and K. Dholakia, "Dual beam fibre trap for Raman micro-spectroscopy of single cells," Opt. Express **14**(12), 5779 (2006).
18. I. T. Leite, S. Turtaev, X. Jiang, M. Šiler, A. Cuschieri, P. S. J. Russell, and T. Čižmár, "Three-dimensional holographic optical manipulation through a high-numerical-aperture soft-glass multimode fibre," Nat. Photonics **12**(1), 33–39 (2018).
19. J. Guck, R. Ananthakrishnan, H. Mahmood, T. J. Moon, C. C. Cunningham, and J. Käs, "The optical stretcher: a novel laser tool to micromanipulate cells," Biophys. J. **81**(2), 767–784 (2001).
20. T. Yang, F. Bragheri, and P. Minzioni, "A comprehensive review of optical stretcher for cell mechanical characterization at single-cell level," Micromachines **7**(5), 90 (2016).
21. P. B. Bareil, Y. Sheng, Y.-Q. Chen, and A. Chiou, "Calculation of spherical red blood cell deformation in a dual-beam optical stretcher," Opt. Express **15**(24), 16029–16034 (2007).
22. P. Y. Liu, L. K. Chin, W. Ser, H. F. Chen, C. M. Hsieh, C. H. Lee, K. B. Sung, T. C. Ayi, P. H. Yap, B. Liedberg, K. Wang, T. Bourouina, and Y. Leprince-Wang, "Cell refractive index for cell biology and disease diagnosis: Past, present and future," Lab Chip **16**(4), 634–644 (2016).
23. M. K. Kreysing, T. Kießling, A. Fritsch, C. Dietrich, J. R. Guck, and J. A. Käs, "The optical cell rotator," Opt. Express **16**(21), 16984–16992 (2008).
24. M. Kreysing, D. Ott, M. J. Schmidberger, O. Otto, M. Schürmann, E. Martín-Badosa, G. Whyte, and J. Guck, "Dynamic operation of optical fibres beyond the single-mode regime facilitates the orientation of biological cells," Nat. Commun. **5**(1), 5481 (2014).
25. A. Sekhar and B. Prabhu, "Effects of coupling misalignment on vibrations of rotating machinery," J. Sound Vibration **185**(4), 655–671 (1995).

26. R. Dasgupta, S. K. Mohanty, and P. K. Gupta, "Controlled rotation of biological microscopic objects using optical line tweezers," Biotechnol. Lett. **25**(19), 1625–1628 (2003).

27. S. Mohanty, R. Verma, and P. Gupta, "Trapping and controlled rotation of low-refractive-index particles using dual line optical tweezers," Appl. Phys. B **87**(2), 211–215 (2007).

28. B. J. Black and S. K. Mohanty, "Fiber-optic spanner," Opt. Lett. **37**(24), 5030–5032 (2012).

29. T. Kolb, S. Albert, M. Haug, and G. Whyte, "Dynamically reconfigurable fibre optical spanner," Lab Chip **14**(6), 1186–1190 (2014).

30. S. Torino, M. Iodice, I. Rendina, G. Coppola, and E. Schonbrun, "A microfluidic approach for inducing cell rotation by means of hydrodynamic forces," Sensors **16**(8), 1326 (2016).

31. M. Schürmann, G. Cojoc, S. Girardo, E. Ulbricht, J. Guck, and P. Müller, "Three-dimensional correlative single-cell imaging utilizing fluorescence and refractive index tomography," J. Biophotonics **11**(3), e201700145 (2018).

32. S. V. Puttaswamy, N. Bhalla, C. Kelsey, G. Lubarsky, C. Lee, and J. McLaughlin, "Independent and grouped 3D cell rotation in a microfluidic device for bioimaging applications," Biosens. Bioelectron. **170**, 112661 (2020).

33. M. Habaza, M. Kirschbaum, C. Guernth-Marschner, G. Dardikman, I. Barnea, R. Korenstein, C. Duschl, and N. T. Shaked, "Rapid 3D refractive-index imaging of live cells in suspension without labeling using dielectrophoretic cell rotation," Adv. Sci. **4**(2), 1600205 (2017).

34. D. Ahmed, A. Ozcelik, N. Bojanala, N. Nama, A. Upadhyay, Y. Chen, W. Hanna-Rose, and T. J. Huang, "Rotational manipulation of single cells and organisms using acoustic waves," Nat. Commun. **7**(1), 11085 (2016).

35. S. P. Zhang, J. Lata, C. Chen, J. Mai, F. Guo, Z. Tian, L. Ren, Z. Mao, P.-H. Huang, P. Li, S. Yang, and T. J. Huang, "Digital acoustofluidics enables contactless and programmable liquid handling," Nat. Commun. **9**(1), 2928 (2018).

36. Y. Kim, S. C. Warren, J. M. Stone, J. C. Knight, M. A. Neil, C. Paterson, C. W. Dunsby, and P. M. French, "Adaptive multiphoton endomicroscope incorporating a polarization-maintaining multicore optical fibre," IEEE J. Sel. Top. Quantum Electron. **22**(3), 171–178 (2016).

37. S. C. Warren, Y. Kim, J. M. Stone, C. Mitchell, J. C. Knight, M. A. Neil, C. Paterson, P. M. French, and C. Dunsby, "Adaptive multiphoton endomicroscopy through a dynamically deformed multicore optical fiber using proximal detection," Opt. Express **24**(19), 21474–21484 (2016).

38. R. Kuschmierz, E. Scharf, N. Koukourakis, and J. W. Czarske, "Self-calibration of lensless holographic endoscope using programmable guide stars," Opt. Lett. **43**(12), 2997–3000 (2018).

39. E. Scharf, J. Dremel, R. Kuschmierz, and J. Czarske, "Video-rate lensless endoscope with self-calibration using wavefront shaping," Opt. Lett. **45**(13), 3629–3632 (2020).

40. J. A. Davis, D. M. Cottrell, J. Campos, M. J. Yzuel, and I. Moreno, "Encoding amplitude information onto phase-only filters," Appl. Opt. **38**(23), 5004–5013 (1999).

41. T. Sarkadi, Á. Kettinger, and P. Koppa, "Spatial filters for complex wavefront modulation," Appl. Opt. **52**(22), 5449–5454 (2013).

42. S. Rothe, H. Radner, N. Koukourakis, and J. W. Czarske, "Transmission matrix measurement of multimode optical fibers by mode-selective excitation using one spatial light modulator," Appl. Sci. **9**(1), 195 (2019).

43. D. Kogan, S. Sivankutty, V. Tsvirkun, G. Bouwmans, E. R. Andresen, H. Rigneault, and D. Oron, "Phase retrieval in multicore fiber bundles," Opt. Lett. **42**(3), 647 (2017).

44. W. Osten, A. Faridian, P. Gao, K. Körner, D. Naik, G. Pedrini, A. K. Singh, M. Takeda, and M. Wilke, "Recent advances in digital holography," Appl. Opt. **53**(27), G44–G63 (2014).

45. W. Saxton, *Computer Techniques for Image Processing in Electron Microscopy*, vol. 10 (Academic Press, 2013).

46. R. Gerchberg, "Holography without fringes in the electron microscope," Nature **240**(5381), 404–406 (1972).

47. J. Sun, N. Koukourakis, and J. W. Czarske, "Complex wavefront shaping through a multi-core fiber," Appl. Sci. **11**(9), 3949 (2021).

48. X. Chen, G. Xiao, K. Yang, W. Xiong, and H. Luo, "Characteristics of the orbital rotation in dual-beam fiber-optic trap with transverse offset," Opt. Express **24**(15), 16952–16960 (2016).

49. X. Chen, G. Xiao, H. Luo, W. Xiong, and K. Yang, "Dynamics analysis of microsphere in a dual-beam fiber-optic trap with transverse offset," Opt. Express **24**(7), 7575–7584 (2016).

50. V. Tsvirkun, S. Sivankutty, K. Baudelle, R. Habert, G. Bouwmans, O. Vanvincq, E. R. Andresen, and H. Rigneault, "Flexible lensless endoscope with a conformationally invariant multi-core fiber," Optica **6**(9), 1185–1189 (2019).

51. J. Lim, K. Lee, K. H. Jin, S. Shin, S. Lee, Y. Park, and J. C. Ye, "Comparative study of iterative reconstruction algorithms for missing cone problems in optical diffraction tomography," Opt. Express **23**(13), 16933–16948 (2015).

52. B. Simon, M. Debailleul, M. Houkal, C. Ecoffet, J. Bailleul, J. Lambert, A. Spangenberg, H. Liu, O. Soppera, and O. Haeberlé, "Tomographic diffractive microscopy with isotropic resolution," Optica **4**(4), 460 (2017).

53. A. Vogel, N. Linz, S. Freidank, and G. Paltauf, "Femtosecond-laser-induced nanocavitation in water: implications for optical breakdown threshold and cell surgery," Phys. Rev. Lett. **100**(3), 038102 (2008).

54. B. Krug, N. Koukourakis, and J. W. Czarske, "Impulsive stimulated brillouin microscopy for non-contact, fast mechanical investigations of hydrogels," Opt. Express **27**(19), 26910–26923 (2019).